Electronic Supplementary Material (ESI) for RSC Advances.

Supplementary Information

Nanoscopic insights into the surface conformation of neurotoxic amyloid β oligomers

Preparation and characterization of $A\beta_{42}$ conformers

According to the first assembly protocol,[1] when maintained in quiescent conditions in PBS at 25 °C, $A\beta_{42}$ monomer rapidly matures into cytotoxic oligomers (A+), which are completely formed after 24 h. After longer incubation times (from 24 h up to 96 h) these oligomers undergo a conformational change to a less toxic oligomeric form (A-) with similar size and morphology. On the other hand, under constant agitation, A+ oligomers directly evolve into fibrils. Specifically, $A\beta_{42}$ powder (Cayman Chemical, USA) was dissolved in 100% hexafluoroisopropanol (Sigma Aldrich, Saint Louis, MO, USA) and stock solutions were stored at -20°C. The solvent was evaporated and $A\beta_{42}$ (1 mg/ml) was dissolved in 50 mM NaOH, sonicated for 30s and diluted in PBS at 25 μM. The peptide was centrifuged at 22,000g for 30 min and the supernatant solution was incubated at 25 °C for 96 h without agitation. The 0-h sample can be considered mostly composed of monomeric $A\beta_{42}$ because it is generally accepted that the treatment of $A\beta_{42}$ with strong alkali such as sodium hydroxide or ammonium hydroxide produces aggregate-free solutions.[2] $A\beta_{42}$ fibrils were prepared with the same procedure except that the concentration for incubation for 24 h at 25 °C was 75 μM.

The preparation of ADDLs was performed as previously reported.[3] Briefly, aliquots of $A\beta_{42}$ were dissolved in DMSO to a final concentration of 5.0 mM, incubated in ice-cold F12 medium to 100 μM at 4 °C for 24 h and then centrifuged at 14,000×g for 10 min. The supernatant, defined as ADDLs preparation, was used for the analyses. Freshly prepared $A\beta_{42}$ solutions kept at 25 °C were used in all the experiments. PolyLys, PolyArg, PolyHis and PolyGlu were purchased from Sigma Aldrich (Saint Louis, MO, USA) and used to prepare solutions at 100 μM concentration in PBS.

A+ oligomers were found to react with the A11 antibody and were negative for the OC antibody (**Fig. S1A**). By contrast, the A- and fibrillar species were negative or very weakly positive for the A11 and positive for the OC antibody, as expected.[1] ADDLs were checked by using the 19.3 anti-ADDLs specific antibody, confirming the specificity of our ADDLs to this antibody (**Fig. S1B**).

Morphology and size of the $A\beta_{42}$ samples were inspected by tapping mode atomic force microscopy (AFM) (**Fig. S1C**). 5 μl $A\beta_{42}$ solution (A+, A- and ADDLs oligomers at 25 μM concentration, $A\beta_{42}$ fibrils at 7 μM concentration) was dried on top of freshly cleaved mica substrates at room temperature for 20 min, followed by rinsing in MilliQ water to remove salts and drying under a gentle nitrogen flow. Samples were immediately imaged using a JPK NanoWizard III Sense (Berlin, Germany) scanning probe microscope operating in AFM mode (maximum z-scan size 15 μm). Single-beam uncoated silicon cantilevers (μMash HQ:NSC15 Cr-Au BS) were used. Drive frequency was between 250 and 300 kHz and the scan rate was 0.5 Hz. Heights in the cross sectional profile were measured**,** appearing to be 4.4±2.4 nm for A+, 4.4±1.5 nm for A- and 3.9±1.2 nm (mean ± SD) for ADDLs, in agreement with previously reported values of 6.2±0.5 nm,[4] 6.1±0.6 nm,[4] and 3.85±0.67 nm,[5] respectively. In the latter case, a SEC fractionation of the high mass oligomers was performed, whereas previous AFM studies using non-fractionated ADDLs allowed to visualize globular oligomers of 5±3 nm.[6, 7] By contrast, fibrils appeared up to few microns in length and 4-6 nm in height, basically confirming previous findings.[4, 8, 9]

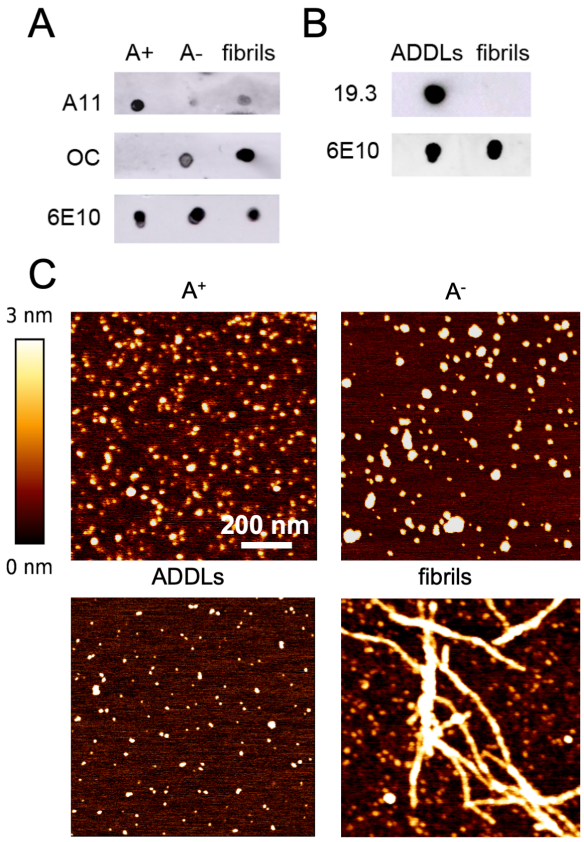

Fig. S1. Characterization of the $A\beta_{42}$ species. A) Dot-blot analysis of A+ and A− oligomers and fibrils (2 µl/spot corresponding to 1 µg in monomer equivalents). Samples were probed with conformation-specific (A11, prefibrillar oligomers, top, and OC, fibrillar conformers, middle) and sequence-specific (6E10, N-terminus of Aβ, bottom) antibodies. B) Dot-blot analysis of ADDLs and fibrils (2 µl/spot corresponding to 1 µg in monomer equivalents). Samples were probed with the ADDL-specific human anti-ADDLs 19.3 therapeutic antibody and the sequence specific 6E10 antibody. C) AFM images of $A\beta_{42}$ oligomers (A+, A-, ADDLs) and $A\beta_{42}$ fibrils, revealing height values of 4.4±2.4 nm for A+, 4.4±1.5 nm for A-, 3.9±1.2 nm for ADDLs.

STED microscopy analysis for the internalization of $A\beta_{42}$ conformers

Authenticated human neuroblastoma SH-SY5Y cells were purchased from A.T.C.C. (Manassas, VA, USA). These cells represent a suitable model system to evaluate the cytotoxic potential of amyloid aggregates, as widely reported in literature for AD.[10] Cells were tested to ensure that they were free form mycoplasma contamination, and were cultured in Dulbecco's Modified Eagle's Medium (DMEM), F-12 Ham with 25mM HEPES and NaHCO3 (1:1) supplemented with 10% fetal bovine serum (FBS), 1.0mM glutamine and 1.0% penicillin and streptomycin solution. Cells were maintained in a 5% CO_2 humidified atmosphere at 37° C and grown until 80% confluence for a maximum of 20 passages. SH-SY5Y cells were differentiated for six days with 10 µM all-*trans* retinoic acid (RA) in their medium supplemented with 1% FBS that was renewed every two days.[11]

Primary rat cortex neurons were purchased from Thermo Fisher Scientific (Waltham, MA, USA), plated and maintained in neuronal basal plus medium (Gibco, Thermo Fisher Scientific) supplemented with GlutaMAX (Gibco) at the concentration of 0.5 mM and 2% (v/v) and a serum-free complement, B-27 (Gibco). Neurons were maintained at 37 °C in a 5.0% CO_2 humidified atmosphere. Every 4 days medium was partially replaced with fresh one. All the experiments were performed 12-16 days after plating, as previously reported.[11]

Differentiated SH-SY5Y cells and $A\beta_{42}$ conformers were labeled as described in **Fig. 1**. Fluoromount-G™ (Thermo Fisher Scientific) was used as mounting medium. STED xyz images (i.e., z-stacks acquired along 3 directions: x, y, and z axes) of differentiated SH-SY5Y cells treated with 3 µM (monomer equivalents) $A\beta_{42}$ conformers (A-, A+, ADDLs or fibrils) were acquired by using an SP8 STED 3X confocal microscope (Leica Microsystems, Mannheim, Germany). The cells were then counterstained with 0.01 mg/ml Tetramethylrhodamine Conjugate of Wheat Germ Agglutinin (Thermo Fisher Scientific, Waltham, MA, USA). $A\beta_{42}$ conformers were detected with 1:125 diluted 1:400 diluted mouse monoclonal anti-$A\beta_{42}$ antibodies (Signet, Dedham, MA, USA) and 1:500 Alexa Fluor 514-goat anti mouse IgG1 secondary antibody (Thermo Fisher Scientific). Fluorescence emission was detected after double excitation at 550 nm and 514 nm. Tetramethylrhodamine fluorophore was excited with a 550 nm-tuned white light laser (WLL) and emission collected from 564 to 599 nm, Alexa Fluor 514 was excited with a 510 nm-tuned WLL and emission collected from 532 to 551 nm. Frame sequential acquisition was applied to avoid fluorescence overlap. It was applied a gating between 0.3 to 6 ns to

avoid collection of reflection and autofluorescence. 650 nm pulsed-depletion laser was used for Alexa Fluor 514 excitation. Images were acquired with Leica HC PL APO CS2 100x/1.40 oil STED White objective. Gated pulsed-STED were applied to Alexa Fluor 514 fluorophore. Collected images were de-convolved with Huygens Professional software version 18.04 (Scientific Volume Imaging B.V., Hilversum, The Netherlands) and analyzed using Leica Application Suite X (LAS X) software (Leica). Images were collected at 0.1 µm intervals.

Cytosolic free Ca^{2+} levels

Primary rat cortex neurons and differentiated SH-SY5Y cells were treated for 15 min with 3 µM (monomer equivalents) $A\beta_{42}$ conformers (A-, A+, ADDLs or fibrils). The cytosolic Ca^{2+} was measured by confocal microscopy by loading the cells with 10 µM Fluo4-AM (Thermo Fisher Scientific), as previously described.[12] Fluorescence emission was detected after excitation at 488 nm by a TCS SP8 scanning confocal microscopy system (Leica Microsystems, Mannheim, Germany), equipped with a diode laser source. A series of 1.0-µm thick optical sections (1024 × 1024 pixels) was taken through the cell depth for each sample using a Leica Plan Apo 63× oil immersion objective, and all sections were projected as a single composite image by superimposition. The confocal microscope was set at optimal acquisition conditions, e.g., pinhole diameters, detector gain and laser powers. The settings were maintained constant for each analysis. 10-22 cells, in three different experiments, were analysed using ImageJ (NIH, Bethesda, MD, USA) software.[13]

MTT reduction test

The cytotoxicity of $A\beta_{42}$ conformers was assessed in differentiated SH-SY5Y cells seeded in 96-well plates by the 3-(4,5-dimethylthiazol-2-yl)-2,5-diphenyltetrazolium bromide (MTT) assay, as previously reported.[11, 13] The cells were treated for 24 h with $A\beta_{42}$ conformers (A-, A+, ADDLs or fibrils, 1 µM, monomer equivalents). Cell viability was expressed as the percentage of MTT reduction in treated cells as compared to untreated cells. The ability of the differentiated SH-SY5Y cells to reduce MTT decreased significantly, by 28±3% and 29±4%, following a 24 h treatment with A+ or ADDLs, respectively, whereas MTT reduction decreased by only 4±1% following cell exposure to A- species. $A\beta_{42}$ fibrils caused a minor but significant decrease of MTT reduction, by 16±2%. Taken together, these results confirm the cytotoxic nature of ADDLs and A+ oligomers and the lack of toxicity of A- oligomers and indicate a differential cytotoxicity behavior displayed by A+ and A- oligomers, which appears related with the way these two conformers interact with the target cells.

Raman spectroscopy

Raman measurements (**Fig. S2**) were carried out under a microRaman setup as previously described.[14] The system is coupled to a 785 nm laser with a 1200 grooves/mm grating. Backscattered light was collected by a 100X objective with 0.9NA which generates a ~1µm laser beam waist and a laser power at the sample of 40 mW. Acquisition time for each spectrum was 20 s with 10 accumulations. A 5 µl drop of $A\beta_{42}$ solution (25 µM) was deposited onto a silver mirror support (Thorlabs) followed by air drying for 20 minutes and acquisition of Raman spectra from the outer ring of the dried drop.

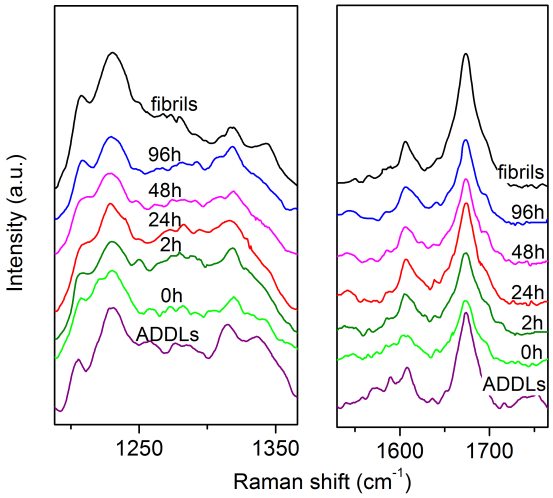

Fig. S2. Raman analysis of $A\beta_{42}$ species. Series of Raman spectra of $A\beta_{42}$ oligomers over 0 h (monomer), 2 h, 24 h, 48 h and 96 h incubation time and of mature fibrils (from bottom to top) in the 1230-1350 cm^{-1} amide III (left) and 1600-1700 cm^{-1} amide I (right) regions. Both amide III and amide I regions of A+, A- oligomers and their intermediate $A\beta_{42}$ conformers as well as ADDLs revealed a similar multicomponent peptide secondary structure composition, closely approaching that of the monomer as a result of a spectral distribution of coexisting bands at comparably low intensities.

AgNWs synthesis

Reagents: Ethylene glycol (EG, 99.5%, Roth), platinum chloride ($PtCl_4$, 99.99+%, Merck), silver nitrate ($AgNO_3$, 99.9% Roth), polyvinylpyrrolidone) (PVP K30, MW 55,000, Aldrich). All chemicals were used without further purification. Preparation: 5÷50 µm long, 70±14 nm thick AgNWs at 5 mg/ml of Ag density were synthesized by a polyol process in the presence of Pt seeds and PVP surfactant. The whole preparation procedure is briefly given as follows. Firstly, 5 ml of pure EG was refluxed in a three-necked round-bottomed flask (equipped with a condenser, thermocontroller, and magnetic stirring bar) at a temperature of about 160 ^{o}C for 1 h. Then 0.5 mL of $PtCl_4$ solution ($1.5x10^{-4}$ M, in EG) was rapidly injected, which caused the Pt seeds to form. After 4 min 2.5 ml EG solution of 0.12 M $AgNO_3$ and 5 ml EG solution of 0.36 M PVP were simultaneously drop-by-drop added by a peristaltic pump into the refluxing EG solution in order to leave AgNWs nucleating and growing on the preformed Pt seeds. The mixture turned yellow as soon as the first drops of $AgNO_3$ and PVP were added, implying the formation of Ag nanoparticles. With continuous injection, the solution became gradually opaque. Vigorous stirring was maintained throughout the entire process. The simultaneous and drop wise addition of $AgNO_3$ and PVP solutions appeared critical to the formation of silver products with wire-like morphology. The product was finally purified by centrifugation or filtration for further characterization by UV-Vis spectroscopy, TEM and EDS (**Fig. S3**).

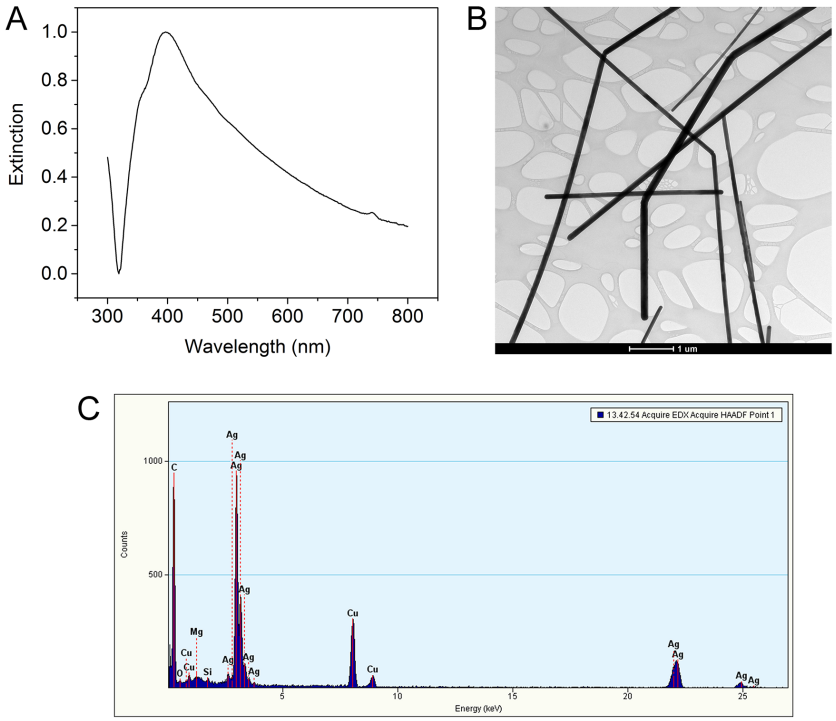

Fig. S3. Characterization of AgNWs. UV-Vis spectrum (A), TEM image (B) and EDS spectrum (C) of AgNWs used to prepare the SERS substrates.

SERS

SERS analysis was performed on spotted networks of AgNWs showing an effective SERS gain of 10^5, high reproducibility (signal fluctuations were estimated ≤ 10% RSD), and a large density of SERS hotspots generated at the gaps between crossed wires, which assure a preferential detection from the outer layers of the $A\beta_{42}$ oligomer (see "FEM simulations" below) and a limit of detection in the micromolar range.[15] AgNWs were 20-time diluted in ethanol and then subjected to filtration under a mild (<400 mbar) pressure through PTFE membranes (0.45 mm pore size, Sartorious GmbH, Goettigen, Germany). AgNWs spots of 2 mm diameter on PTFE membranes were fabricated in wet irradiation conditions by a selective laser ablation technique. The second harmonic (532 nm) of a ns-pulsed Nd:YAG laser (Quantel CFR400) was coupled into a quartz optical fiber to form a nearly flat-top (top-hat) beam output. Suitable optics and spatial filtering were then used in 1:1 imaging configuration to generate annular ablation patterns on PTFE membrane. In detail, the collimated output laser beam (Ø= 6 mm) of a Q-Switched Nd:YAG laser equipped with 2nd harmonic generator (532 nm, 8 ns pulse duration, 200 mJ maximum pulse energy) was coupled into a quartz optical fiber (1.5 mm core diameter, 30 m fiber length) through L1 lens of 100 mm focal length. L2 lens (25 mm focal length) was used for collimating the nearly flat-top (top-hat) beam at the fiber output. After this collimation, the beam had a diameter of about 7.5 mm. Then, the cross-section of the laser beam was spatially re-shaped using an annular aperture whose outer and inner (obstruction) diameters were 9 and 4 mm, respectively. A bi-convex spherical lens (L3) of 30 mm focal length was finally placed at 2*f* (i.e. two times the focal length) in order to achieve a 1:1 image of the aperture onto the AgNWs-coated PTFE membrane. In this way, above a fluence

threshold of 200 mJ/cm^2, an annular ablation spot of the AgNWs film was achieved, as shown in **Fig. S4**. Operatively, each AgNWs-coated PTFE membrane was placed into a sterilized glass Petri dish (50 mm diameter) previously filled with 5 ml ethanol (96% v/v for analysis, ACS). After being completely wet, the PTFE membrane was processed using optimized irradiation parameters, which were found to be 200-250 mJ/cm^2 fluence range, 2Hz pulse repetition frequency and 30 laser pulses for complete removal of the AgNWs film. Constant immersion during the experiment helped to reduce the thermal load to the PTFE membrane. The output laser energy was measured by means of an in-line energy meter (EM) and finely adjusted using neutral density filters (NDF). Finally, a number of 10 AgNWs spot on each PTFE membrane were obtained by translation of the latter with a long-travel XY stage.

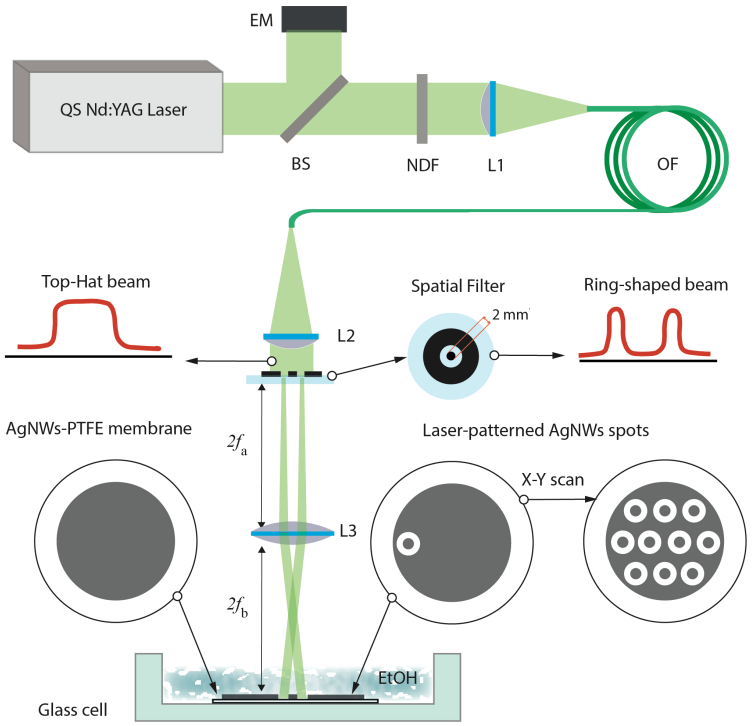

Fig. S4. Schematic diagram illustrating the fabrication of AgNWs spots on PTFE membranes by selective laser ablation. From top to bottom: QS Nd:YAG (532 nm wavelength, 8 ns pulse duration) laser, dichroic mirror (BS), energy meter (EM), attenuating filter (NDF), plano-convex coupling lens (L1), optical fiber (OF), collimating lens (L2), spatial filter, imaging lens (L3).

The morphology of the substrate was finally analyzed by tapping mode AFM (JPK NanoWizard III Sense, Berlin, Germany) Contact angle measurements were conducted on a custom setup on 5 µl aqueous solutions placed on the top of a AgNWs spot.
SERS measurements were carried out under the same setup used for Raman spectroscopy. The backscattered light was collected by a 10X objective with 0.25NA which generated a ~7µm large laser beam waist at 600 µW. 5 µl of Aβ_{42} solution (1 µM) was deposited on the AgNWs spot followed by air drying for 15 minutes and acquisition of SERS spectra from the dried drop throughout the area of the spot was carried out. 10 s of integration time and single accumulations were used and each spectrum represented an average of a minimum of 30 spectra collected by mapping experiments over 12 mm^2 areas with step size of 100 µm. The above strategy assured to minimize possible signal variability.[16-18] A baseline correction by polynomial fitting and smoothing was applied to the spectra. We note that, on the opposite of standard Raman spectroscopy, amide III and amide I signals appear to have undetectable or low intensity and are thus scarcely informative in SERS spectra of protein species, which is a consequence of a location of peptide backbone buried by bulky side chains shielding their SERS information.[19, 20]

FEM simulations

We used a commercial FEM package, the wave optical module of COMSOL multiphysics (v 5.1) to simulate the electric field distribution in the near proximity of the AgNWs. We chose to depict the nanowire as a cylinder with smoothed pointy ends, with radius 40 nm and total length 5 µm. The refractive index of the silver of AgNW was taken from Rakić et al.,[21] while that of the surroundings of the wire was fixed at 1. AgNWs were illuminated by a 785 nm plane wave and linear polarization and different angles for both propagation direction and polarization of the incident electromagnetic radiation were considered. In general, incident light polarizes the ends and gives rise to a standing surface charge wave along the wire.[22] Unlike nanorods and nanoparticles, nanowires exhibit higher order modes due to their relatively significant dimensions with respect to the illumination wavelength. A prevailing assembly of the AgNWs in the form of a random network of intertwined nanoparticles emerges by AFM inspection (**Fig. S5A**), which can be quantified in an almost 100% of the wires. This network features a large density of SERS hotspots generated at the gaps between crossed wires, which we quantified ~10/µm^2. We may note that the intersections formed

by crossed AgNWs were previously indicated as the configuration showing the highest SERS enhancement surpassing that of the isolated counterpart due to a strong plasmon coupling effect.[23] These hotspots account for a maximum $|E|/|E_0|$ ~5 when 90°-crossed AgNWs are considered (**Figs. S5B,C**), rapidly decaying on moving away as shown in **Fig. S5D**. A 4÷5 nm in size oligomer placed at the hotspot (**Fig. S5D inset**) will not be able to fully enter the intersection volume formed between crossed AgNWs but will remain at a distance that we can estimate equal to ~15 nm from the crossing point. As a consequence it features a strong decreasing enhancement factor (EF) from the edges towards the inside structures, which can be quantified in a 46% reduction (red band in **Fig. S5D)** passing from one to the other oligomer side. Being SERS intensity proportional to the EF, we can assume a decrease in SERS signals of at least 24% between the exposed surface and the core of the oligomer. In conclusion the SERS signals obtained by using our SERS assay (as those presented in **Fig. 2E** and **Fig. 3**) are expected to provide a preferential description of the outer layers of the $A\beta_{42}$ oligomer.

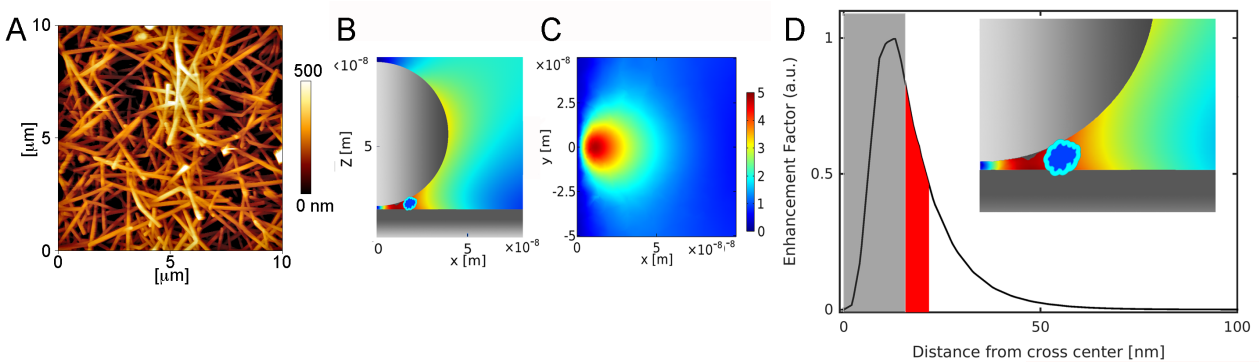

Fig. S5. FEM modeling of the E-field distribution. A) AFM image of the AgNWs network of the SERS substrates used in this work. 2D sections xz in B) and xy in C) of FEM simulations of the E-field intensity (|E|/|E0|) in-between two crossed AgNWs in air. D) Profile of EF along the x-direction. Access to the gray zone adjacent to the origin of the intersection, from 0 to ~15 nm, is denied to the oligomer due to steric impediments, while the zone highlighted in red shows the EF decrease experienced by a 4 nm sized molecule as close as possible to the hot spot (as displayed in **Fig. S5D inset**).

Multipeak fitting

A multipeak fitting procedure with Lorentzian curves was finally carried out on selected spectral regions and the integrated areas or the maximum intensity values of the fitted peaks were collected and analyzed. Specifically, the multi-peak fit procedure of Igor Pro 6.0 software (Wavemetrics, Inc.) with Lorentzian peak fit provided the real location of the peak, the real amplitude, the area and Full Width at Half Maximum (FWHM) for each peak, as well as estimated errors for each quantity. A typical multipeak fit result is reported in the figure below for Tyr bands at 830 cm^{-1} of and 850 cm^{-1} of A- species.

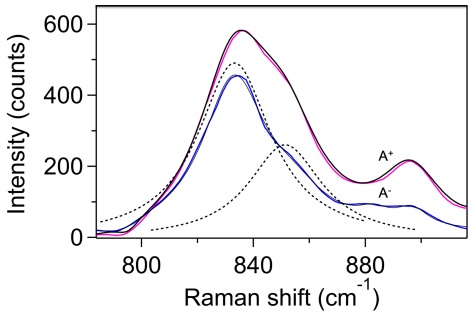

Fig. S6. Deconvolution analysis of Tyr bands for the toxic A+ oligomer (pink) through a multipeak fit procedure with Lorentzian functions. The SERS spectrum of the non-oxic A- oligomer (blue) is shown for comparison.

SERS analysis

Table S1. Assignments of SERS signals of Aβ species[24-27]

Peak position (cm^{-1})	Assignment	
830	ring	Tyr
850	ring	Tyr
897	C-C str	
935	C-C str	
1003	sym ring breath	Phe
1032	in-plane CH bend	Phe
1047-1130	CN str	
1162	NH_3^+ def	
1205	phenyl-C str	Phe
1420-1460	CH_2,CH_3 def	
1583, 1604, 1617	ring	Phe, Tyr
1680	Amide I	

MD simulations

The structural models for $A\beta_{42}$ oligomers available in the literature are mainly extracted from fibril-like assemblies,[28-30] being the latter the only structures available as initial states for any fitting procedure.[31, 32] Here we used oligomer structures obtained by MD simulations in room conditions that started from monomer and dimer structures simulated in water solution.[33, 34] These oligomers are characterized by a low extent of β-strand structure, the latter condition more representative of the A+ state. The models are characterized by an average gyration radius of about 2 nm and, thus, a size of about 4 nm, matching the average size of the $A\beta_{42}$ oligomers considered in our experiments. The method used is based on the statistics of empirical models obtained by computational methods and described in Refs[33, 34]. Finally five tetramer assemblies were selected on the basis of a calculated R-value (see below), which mainly derive from the assembly of elongated dimers. Even though this organization is partially due to the initial conditions used for the simulation, we can speculate that tetramers start aggregating from dimers characterized by the longest lifetime (i.e. those with the highest population).

Sampling can be summarized as follows in detail. Initial configurations of $A\beta_{42}$ were selected as the most representative structures obtained with 1 μs-long MD simulations.[34] For instance, when monomers were required to build dimers, we extracted from the simulations of monomers the first configuration with gyration radius (R_g) and solvent accessible surface area (SASA) corresponding to the maximum of the population for these variables obtained with the entire simulation. The same selection of initial configurations was adopted for dimers when the latter were used in the construction of tetramers. Therefore, the selection of initial configurations was performed according to the maximally populated peak in the R_g/ SASA map in all cases. The force field used in simulations was Amber 99SB.[35] We built different assemblies of A and B monomers into AB dimers, and of AB and CD dimers into tetramers. This was done by placing in space two particles, monomers and dimers, for building dimers and tetramers, respectively. We placed the particles with the selected structures and with random orientations with centers of mass at an approximate distance of 2 nm. The particles were inserted into orthorhombic simulation cells filled of water molecules described as in the TIP3P model and a neutralizing amount of NaCl.

We performed MD simulations in steps of 1 ns in the NPT statistical ensemble of 128 initial mutual orientations of the particles. Pressure was 1 bar and temperature was 300 K. We used the multiple-walkers metadynamics to separate the independent trajectories, one with respect to each other. The diversity among different walkers is here limited to the mutual orientation of the peptide that form each assembly: monomers, when dimers are built; dimers, when tetramers are built. We performed a single multiple-walkers simulations for 128 replica of the system. The spreading of walkers among independent trajectories was performed by adding a bias potential constructed according to the altruistic method,[36] with a collective variable chosen as the number of salt bridges within each monomer. This choice was dictated by the observation that this variable is particularly effective in changing the peptide structure,[34] thus allowing a wider sampling of different structures within the multiple walkers. After MD simulation of 20 ns in the presence of the progressively built (history dependent) bias, 2 ns were performed with no bias. The last 1 ns was used for averaging, using one configuration every 10 ps of simulation (100 configurations per walker). The NAMD 2.10 package[37] was used for the simulations, with most of the MD simulation parameters chosen according to standard procedures.

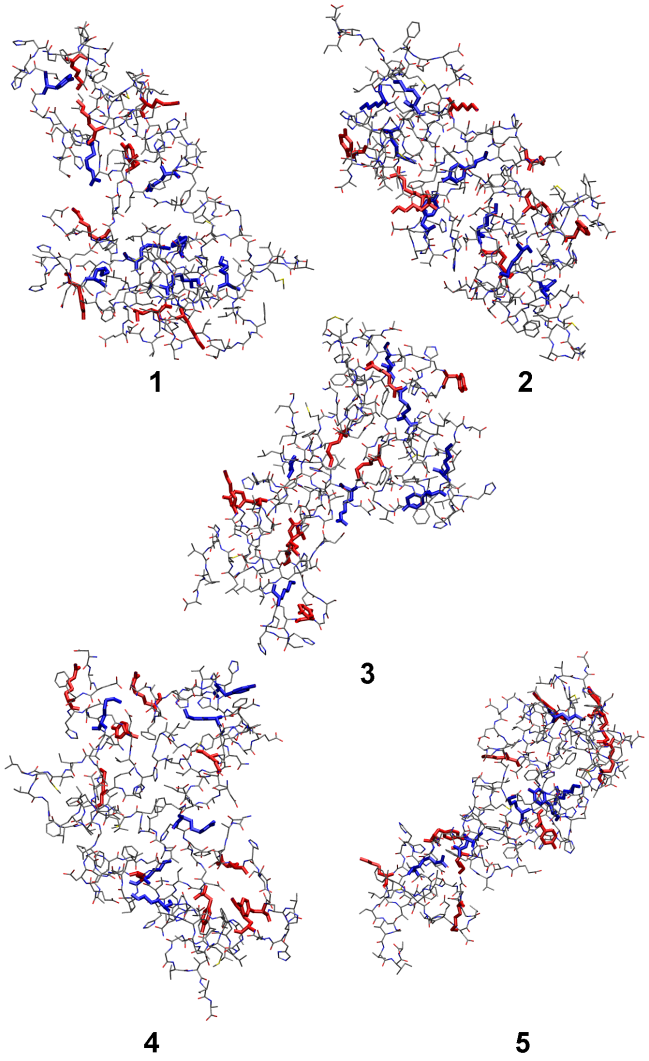

Fig. S7. Representative structures of compact (R<0.9, see text for definition) $A\beta_{42}$ oligomers. Minimal root-mean square deviation between displayed backbone structures is in the range 1-2 nm. Tyr, Lys and Arg side chains are emphasized in boldface. Side chains of Tyr10, Lys16, Lys28 and Arg5 with relative accessibility to water rSASA>0.3 (see text) are in red, while those with rSASA<0.3 are in blue. SASA is the average value for each side chain within the pool of structures belonging to each cluster. Bond radii are arbitrary.

Tetramers were selected according to the R parameter defined as:

$$R = \frac{SASA_{oligo}}{[SASA_{AB} + SASA_{CD}]} \quad (1)$$

where A-D identify different $A\beta_{42}$ monomers, $SASA_{oligo}$ (solvent-accessible surface area of the oligomer) is calculated with a numerical method[38] and AB and CD are preorganized dimers obtained by long (μs) simulations (see above). Structures with R <0.9 can be represented by 5 different compact oligomers that are displayed in **Fig. S7**. About 80% of Lys28 and Tyr10 side chains appeared accessible to water and thus foreseen as potentially available for interaction with the silver surface of the SERS substrate (**Table S2**). Conversely an accessibility to water < 50% was predicted for Arg5 and Lys16. Interestingly, while Lys28 appears mostly accessible in our oligomeric structures, it was previously shown to be involved in intramolecular salt bridges with Glu22 and Asp23 of fibrillar configurations, sealing this residue into a buried position.[39, 40] The above picture is here confirmed by comparing relative SASA values from our oligomers and fibrils where relative SASA represents the ratio between SASA values from atoms of the side chains of $A\beta_{42}$ assemblies and maximal SASA values of the same atoms in $A\beta_{42}$ monomers, or:

$$rSASA_{fibril} = \frac{SASA_{fibril}}{SASA_{monomer}} \quad (2)$$

$$rSASA_{oligo} = \frac{SASA_{oligo}}{SASA_{monomer}} \quad (3)$$

For this purpose we selected the PDB structure 5OQV as a fibril model, as it is the only one including the N-terminus.[41] The average over the nine chains constituting a single fiber ($SASA_{fibril}$) and the maximal value among the A-D chains of the tetramer ($SASA_{oligo}$) are considered in Eq. (2) and (3) in the case of fibrils and $A\beta_{42}$ tetramers, respectively. $rSASA_{oligo}$ = 0.50 *vs.* $rSASA_{fibril}$ = 0.18 for Lys28 and $rSASA_{oligo}$ = 0.46 *vs.* $rSASA_{fibril}$ = 0.37 for Tyr10 were found, which outlines a substantial decrease in water accessibility of these residues when involved in a fibrillar architecture while a large solvent availability in the oligomer form is anticipated. Lys16 and Arg5 showed similar rSASA values <0.40 irrespective of the assembly form considered, which is in line with residues with scarce mobility due to structural constrains and buried within the core of both fibrillar and oligomeric assemblies. These considerations allow further confining the results of our investigation to a precise aminoacid selection, being Lys28 and Tyr10 preferred over the others in establishing aberrant interactions with neurons.

Table S2. Summary of solvent accessibility of Tyr, Lys and Arg sidechains in $A\beta_{42}$ simulated compact tetramers, i.e. when the assembly parameter R is lower than 0.9. Chains are indicated with A, B, C, and D. Side chains are accessible (+) when the solvent accessible surface area (SASA) of each side chain is larger than 30% of the maximal sampled value among corresponding chains in monomeric state (R=1).

Structure	Tyr 10				Lys 16				Lys 28				Arg 5			
	A	B	C	D	A	B	C	D	A	B	C	D	A	B	C	D
1	-	+	+	-	-	-	-	-	+	+	+	-	-	+	+	-
2	+	+	-	+	+	+	+	-	+	+	-	-	+	-	+	+
3	-	+	+	+	+	-	-	-	+	+	+	+	-	+	-	-
4	+	+	+	+	-	+	+	-	+	-	-	+	+	+	+	-
5	-	+	+	+	-	-	-	+	+	+	+	+	+	-	-	-

References

1 R. W. Hepler, K. M. Grimm, D. D. Nahas, R. Breese, E. C. Dodson, P. Acton, P. M. Keller, M. Yeager, H. Wang, P. Shughrue, G. Kinney and J. G. Joyce, *Biochemistry*, 2006, **45**, 15157-15167.

2 T. M. Ryan, J. Caine, H. D. T. Mertens, N. Kirby, J. Nigro, K. Breheney, L. J. Waddington, V. A. Streltsov, C. Curtain, C. L. Masters and B. R. Roberts, *PeerJ*, 2013, **1**.

3 M. P. Lambert, A. K. Barlow, B. A. Chromy, C. Edwards, R. Freed, M. Liosatos, T. E. Morgan, I. Rozovsky, B. Trommer, K. L. Viola, P. Wals, C. Zhang, C. E. Finch, G. A. Krafft and W. L. Klein, *Proc. Natl. Acad. Sci. U.S.A.*, 1998, **95**, 6448-6453.

4 A. R. A. Ladiwala, J. Litt, R. S. Kane, D. S. Aucoin, S. O. Smith, S. Ranjan, J. Davis, W. E. Van Nostrand and P. M. Tessier, *J. Biol. Chem.*, 2012, **287**, 24765-24773.

5 A. Sebollela, G. M. Mustata, K. Luo, P. T. Velasco, K. L. Viola, E. N. Cline, G. S. Shekhawat, K. C. Wilcox, V. P. Dravid and W. L. Klein, *ACS Chem. Neurosci.*, 2014, **5**, 1238-1245.

6 B. A. Chromy, R. J. Nowak, M. P. Lambert, K. L. Viola, L. Chang, P. T. Velasco, B. W. Jones, S. J. Fernandez, P. N. Lacor, P. Horowitz, C. E. Finch, G. A. Krafft and W. L. Klein, *Biochemistry*, 2003, **42**, 12749-12760.

7 G. M. Mustata, G. S. Shekhawat, M. P. Lambert, K. L. Viola, P. T. Velasco, W. L. Klein and V. P. Dravid, *Appl. Phys. Lett.*, 2012, **100**, 4.

8 W. B. Stine, S. W. Snyder, U. S. Ladror, W. S. Wade, M. F. Miller, T. J. Perun, T. F. Holzman and G. A. Krafft, *J. Protein Chem.*, 1996, **15**, 193-203.

9 T. Watanabe-Nakayama, K. Ono, M. Itami, R. Takahashi, D. B. Teplow and M. Yamada, *Proc. Natl. Acad. Sci. U.S.A.*, 2016, **113**, 5835-5840.

10 S. I. Cohen, S. Linse, L. M. Luheshi, E. Hellstrand, D. A. White, L. Rajah, D. E. Otzen, M. Vendruscolo, C. M. Dobson and T. P. Knowles, *Proceedings of the National Academy of Sciences of the United States of America*, 2013, **110**, 9758-9763.

11 R. Cascella, E. Evangelisti, A. Bigi, M. Becatti, C. Fiorillo, M. Stefani, F. Chiti and C. Cecchi, *J. Alzheimers Dis.*, 2017, **60**, 923-938.

12 M. V. Vega, R. Cascella, S. W. Chen, G. Fusco, A. De Simone, C. M. Dobson, C. Cecchi and F. Chiti, *ACS Chem. Biol.*, 2019, **14**, 1593-1600.

13 C. Gellini, G. Sabatino, A. M. Papini and M. Muniz-Miranda, *J. Raman Spectrosc.*, 2014, **45**, 418-423.

14 P. Matteini, M. Cottat, F. Tavanti, E. Panfilova, M. Scuderi, G. Nicotra, M. C. Menziani, N. Khlebtsov, M. de Angelis and R. Pini, *ACS Nano*, 2017, **11**, 918-926.

15 M. Banchelli, C. Amicucci, E. Ruggiero, C. D'Andrea, M. Cottat, D. Ciofini, I. Osticioli, G. Ghini, S. Siano, R. Pini, M. de Angelis and P. Matteini, *ChemNanoMat*, 2019, **5**, 1036-1043.

16 H. Ma, X. Tang, Y. Liu, X. X. Han, C. He, H. Lu and B. Zhao, *Analytical chemistry*, 2019, **91**, 8767-8771.
17 D. Karthigeyan, S. Siddhanta, A. H. Kishore, S. S. Perumal, H. Agren, S. Sudevan, A. V. Bhat, K. Balasubramanyam, R. K. Subbegowda, T. K. Kundu and C. Narayana, *Proc Natl Acad Sci U S A*, 2014, **111**, 10416-10421.
18 B. Della Ventura, M. Banchelli, R. Funari, A. Illiano, M. De Angelis, P. Taroni, A. Amoresano, P. Matteini and R. Velotta, *Analyst*, 2019, **144**, 6871-6880.
19 D. Kurouski, R. P. Van Duyne and I. K. Lednev, *Analyst*, 2015, **140**, 4967-4980.
20 C. Blum, T. Schmid, L. Opilik, N. Metanis, S. Weidmann and R. Zenobi, *J. Phys. Chem. C*, 2012, **116**, 23061-23066.
21 A. D. Rakic, A. B. Djurisic, J. M. Elazar and M. L. Majewski, *Applied optics*, 1998, **37**, 5271-5283.
22 L. Novotny, *Physical review letters*, 2007, **98**, 266802.
23 A. R. Tao and P. Yang, *The journal of physical chemistry. B*, 2005, **109**, 15687-15690.
24 E. Podstawka, Y. Ozaki and L. M. Proniewicz, *Appl. Spectrosc.*, 2004, **58**, 1147-1156.
25 S. Stewart and P. M. Fredericks, *Spectrochim. Acta A Mol. Biomol. Spectrosc.*, 1999, **55**, 1615-1640.
26 E. Podstawka, Y. Ozaki and L. M. Proniewicz, *Appl. Spectrosc.*, 2004, **58**, 570-580.
27 G. D. Chumanov, R. G. Efremov and I. R. Nabiev, *J. Raman Spectrosc.*, 1990, **21**, 43-48.
28 M. Kloniecki, A. Jablonowska, J. Poznanski, J. Langridge, C. Hughes, I. Campuzano, K. Giles and M. Dadlez, *J. Mol. Biol.*, 2011, **407**, 110-124.
29 L. Gu, C. Liu, J. C. Stroud, S. Ngo, L. Jiang and Z. F. Guo, *J. Biol. Chem.*, 2014, **289**, 27300-27313.
30 A. M. Brown and D. R. Bevan, *Biophys. J.*, 2016, **111**, 937-949.
31 L. P. Yu, R. Edalji, J. E. Harlan, T. F. Holzman, A. P. Lopez, B. Labkovsky, H. Hillen, S. Barghorn, U. Ebert, P. L. Richardson, L. Miesbauer, L. Solomon, D. Bartley, K. Walter, R. W. Johnson, P. J. Hajduk and E. T. Olejniczak, *Biochemistry*, 2009, **48**, 1870-1877.
32 B. Chandra, D. Bhowmik, B. K. Maity, K. R. Mote, D. Dhara, R. Venkatramani, S. Maiti and P. K. Madhu, *Biophys. J.*, 2017, **113**, 805-816.
33 G. La Penna and M. S. Li, *Phys. Chem. Chem. Phys.*, 2019, **21**, 8774-8784.
34 P. D. Q. Huy, Q. V. Vuong, G. La Penna, P. Faller and M. S. Li, *ACS Chem. Neurosci.*, 2016, **7**, 1348-1363.
35 V. Hornak, R. Abel, A. Okur, B. Strockbine, A. Roitberg and C. Simmerling, *Proteins*, 2006, **65**, 712-725.
36 P. Hosek, D. Toulcova, A. Bortolato and V. Spiwok, *The journal of physical chemistry. B*, 2016, **120**, 2209-2215.
37 J. C. Phillips, R. Braun, W. Wang, J. Gumbart, E. Tajkhorshid, E. Villa, C. Chipot, R. D. Skeel, L. Kale and K. Schulten, *Journal of computational chemistry*, 2005, **26**, 1781-1802.
38 F. Eisenhaber, P. Lijnzaad, P. Argos, C. Sander and M. Scharf, *J. Comput. Chem.*, 1995, **16**, 273-284.
39 W. Xi and U. H. E. Hansmann, *The Journal of chemical physics*, 2018, **148**, 045103.
40 W. Qiang, W. M. Yau, Y. Luo, M. P. Mattson and R. Tycko, *Proc. Natl. Acad. Sci. U.S.A.*, 2012, **109**, 4443-4448.
41 L. Gremer, D. Scholzel, C. Schenk, E. Reinartz, J. Labahn, R. B. G. Ravelli, M. Tusche, C. Lopez-Iglesias, W. Hoyer, H. Heise, D. Willbold and G. F. Schroder, *Science*, 2017, **358**, 116-+.